

Generate the Forest before the Trees - A Hierarchical Diffusion model for Climate Downscaling

Declan J. Curran^{*,1}, Sanaa Hobeichi^{†,2}, Hira Saleem^{‡,1}, Hao Xue^{§,1}, and Flora D. Salim^{¶,1}

¹School of Computer Science and Engineering, University of New South Wales, Sydney, New South Wales, Australia

²ARC Centre of Excellence for the Weather of the 21st Century and Climate Change Research Centre, University of New South Wales, Sydney, New South Wales, Australia

Abstract

Downscaling is essential for generating the high-resolution climate data needed for local planning, but traditional methods remain computationally demanding. Recent years have seen impressive results from AI downscaling models, particularly diffusion models, which have attracted attention due to their ability to generate ensembles and overcome the smoothing problem common in other AI methods. However, these models typically remain computationally intensive. We introduce a Hierarchical Diffusion Downscaling (HDD) model, which introduces an easily-extensible hierarchical sampling process to the diffusion framework. A coarse-to-fine hierarchy is imposed via a simple downsampling scheme. HDD achieves competitive accuracy on ERA5 reanalysis datasets and CMIP6 models, significantly reducing computational load by running on up to half as many pixels with competitive results. Additionally, a single model trained at 0.25° resolution transfers seamlessly across multiple CMIP6 models with much coarser resolution. HDD thus offers a lightweight alternative for probabilistic climate downscaling, facilitating affordable large-ensemble high-resolution climate projections. See a full code implementation at: <https://github.com/HDD/HDD-Hierarchical-Diffusion-Downscaling>.

1 Introduction

High resolution earth system data is critical for understanding and mitigating the impacts of anthropogenic climate change; however, it is too computationally expensive to do this with traditional methodologies on a large-scale [8] [26]. For example, general circulation models (GCMs) exhibit at least $\mathcal{O}(n^3)$ complexity with respect to resolution of the climate model due to the processing of variables in three dimensions [2] [1] [8]. This means that often, important future and historical climate datasets are not able to be used for local planning or only a limited subset of models are used, meaning the full distribution of potential future climate outcomes are not being covered [28] [26] [8]. For instance, we note that only 2/5 Shared Socioeconomic Pathways (SSPs) of the IPCC’s 6th Assessment Report have been downscaled to high resolutions—leaving large parts of the potential future climate distribution unavailable[28].

*d.curran@unsw.edu.au

†s.hobeichi@unsw.edu.au

‡h.saleem@unsw.edu.au

§hao.xue1@unsw.edu.au

¶flora.salim@unsw.edu.au

In recent years, earth system modelling has undergone vast improvements owing to the proliferation of AI and advancements in computer science [3][22][20][7]. Results from machine learning models in various earth-science tasks⁶ are often competitive or better on various metrics, but at a fraction of the inference cost [3][7]. Downscaling particularly, has seen various promising advancements [23] but these are rarely compared against results from existing dynamical models and climate metrics which renders their practical use quite limited for climate scientists.

Additionally, recent advances in computer vision have led to significant progress in auto-regressive image generation, with models such as VAR and GPT-4o demonstrating state-of-the-art performance [33] [5]. These models exhibit favorable scaling properties and excel in generating high-fidelity images by modeling pixel or patch sequences auto-regressively. Despite their success, such approaches remain largely unexplored in weather and climate image generation, primarily due to the computational complexity and the challenges of capturing spatiotemporal consistency and physical realism required in geoscientific applications.

A small but growing subset of the literature has examined the concept of dimension destruction in diffusion models [16] [38] [4]; in addition to corrupting the training images with gaussian noise, the dimension or size of the image is destroyed gradually. We present an easily extensible addition to the noise process which can be added to an existing diffusion model. By encouraging the model to learn at different resolutions, we construct a hierarchical schedule that downscales autoregressively in a coarse to fine manner. We show that this framework can be easily applied to most existing diffusion model setups with some minor adjustments⁷. We also show that these models produce results competitive with and occasionally exceeding traditional dynamically downscaled models that have used nested RCMs within a GCM—these results are achieved over the Australian domain for a fraction of the inference/training cost.

1. We propose HDD (Hierarchical Diffusion Downscaling), a model which learns multi-scale representations via a hierarchical diffusion process. It applies dimension destruction with noise injection to enable robust feature learning across resolutions, followed by a coarse-to-fine reverse generation during inference. HDD is trained over varying spatial shapes to enforce scale consistency and improve high-resolution reconstruction.
2. Our proposed methodology is architecture-agnostic, allowing integration with any existing diffusion model by augmenting it with shape-conditioning resulting in resolution-aware conditioning mechanism. The framework supports plug-and-play usage within standard diffusion pipelines, making it broadly applicable to weather and climate models without architectural re-design.
3. We train our model on ERA5 over the Australian domain and provide a comprehensive evaluation benchmark with climate metrics. The proposed model passes all climate evaluation metrics and is competitive with other AI/traditional dynamical earth models despite a significantly reduced computational cost.

2 Related Work

Diffusion models implicitly generate images in a coarse to fine manner [9] [29]. This is consistent with the way that humans process images where coarse features are processed first followed by finer details—i.e. we ‘see’ the forest before the trees[13] [25] [24] [18].

Many atmospheric variables also exhibit these same power laws [37], analogous to the $1/f$ fractal spectra of natural images [34] [14]. This indicates variability across scales, with dominant energy at larger scales but a continuous scale-invariant distribution down to finer scales. For example, the Nastrom–Gage spectrum, derived from global aircraft data, demonstrates a robust kinetic energy scaling from approximately 3000 km to several kilometers, following k^{-3} at larger scales transitioning to $k^{-5/3}$ at smaller scales [11].

Regional analyses, including high-resolution reanalyses (e.g., ERA5 at 0.25°) and radar observations, also confirm this $1/f$ -like spectral behavior in atmospheric variables, such as precipitation intensity. These observations reveal continuous cascades from large storm systems down to small-scale showers

⁶Weather prediction, Downscaling, Climate Emulation and many more

⁷See methodology in section 3 for more details

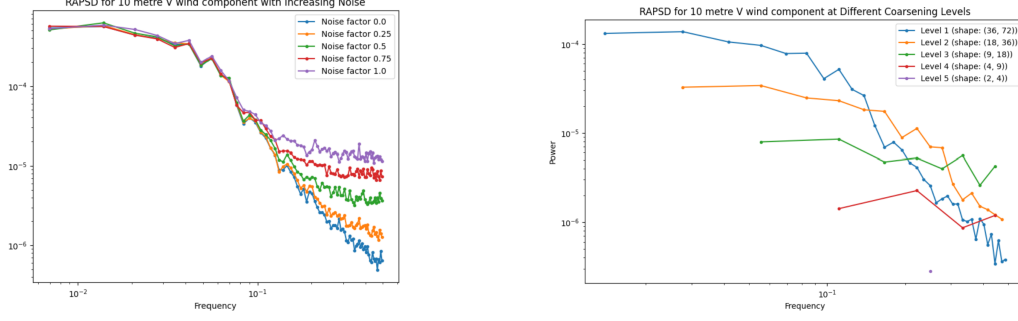


Figure 1: Left: High frequency finer features are the first to be corrupted by random noise. Conversely, the reverse diffusion process generates in a coarse to fine manner implicitly which is partially responsible for their impressive image generation capabilities. However, we find that we can improve results further by enforcing this coarse-to-fine relationship explicitly. Right: Weather data exhibits a clear power law. Coarser features are much less information dense and closer to random noise. It is therefore, easier to model the coarser manifold first, and progressively model higher frequency details. See appendix B for further information on this

without distinct breaks in scaling, consistent with findings from convection-permitting model forecasts in the U.S [12].

The presence of self-similar, power-law spectra strongly motivates the application of coarse-to-fine multi-scale methods in atmospheric modeling and downscaling. Techniques like RainFARM exploit these scaling laws, generating fine-scale structures consistent with prescribed spectral properties, thereby reinforcing the conceptual and practical alignment between diffusion models in machine learning and traditional fractal-based atmospheric downscaling approaches [27] [10].

3 Methodology

We impose an **explicit coarse-to-fine hierarchy** on the outputs of a noise-conditioned diffusion model by coupling the usual Gaussian noising process with a progressive *down-sampling* / *up-sampling* schedule that is sampled at every training step (see accompanying figure).

3.1 Baseline EDM formulation

We use a baseline implementation from [36] of the original EDM paper from NVIDIA[17] which formalises and consolidates terminology from different diffusion methodologies. Refer to the full paper [17] for further details but the basic setup is as follows:

Let $x_0 \in \mathbb{R}^{H \times W \times C}$ be a clean image and let $\{\sigma_t\}_{t=1}^T$ be a monotonically *increasing* noise schedule with $\sigma_0=0$.

1. a *forward* (noising) kernel

$$q(x_t | x_{t-1}) = \mathcal{N}(x_t; x_{t-1}, \sigma_t^2 I), \quad t = 1, \dots, T,$$

2. and a learnable *reverse* kernel

$$p_\theta(x_{t-1} | x_t, \sigma_t) = \mathcal{N}(x_{t-1}; \mu_\theta(x_t, \sigma_t), \sigma_t^2 I),$$

where μ_θ is the output of a score network trained to minimise the EDM loss.

3.2 Adding spatial hierarchies

Denote by $\mathbf{s}_t = (h_t, w_t)$ the *target resolution* at step t , with $(h_0, w_0) = (H, W)$ and $(h_T, w_T) \approx (1, 1)$. For each resolution we define

$$D_{\mathbf{s}_t} : \mathbb{R}^{h_{t-1} \times w_{t-1} \times C} \longrightarrow \mathbb{R}^{h_t \times w_t \times C}, \quad U_{\mathbf{s}_t} : \mathbb{R}^{h_t \times w_t \times C} \longrightarrow \mathbb{R}^{h_{t-1} \times w_{t-1} \times C},$$

as bilinear *down-sampling* and matching *up-sampling* operators, respectively.

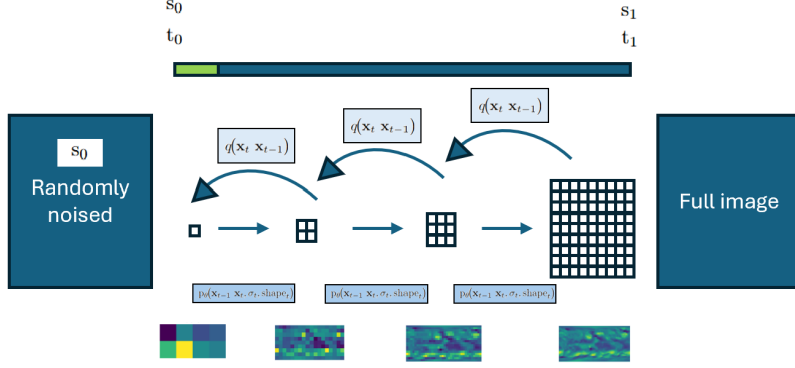


Figure 2: In training, the destruction kernel $q()$ progressively adds noise to an image and gradually destroys dimensions according to the shape scheduler. At inference, the UNET $p()$ learns the inverse of this destruction kernel to produce probabilistic downscaled results that match the initial distribution. Note that although a UNET is used for $p()$ here, any function approximator can be used to replicate this process. Not only is this process intuitive for image processing, we also show that competitive results can be achieved with up to half the pixels processed at inference in the climate setting.

Hierarchical reverse process. The network is trained to *simultaneously denoise and un-coarsen*. Conditioning on both σ_t and the shape s_t we write

$$q(x_t | x_{t-1}) = \mathcal{N}(x_t; x_{t-1}; s_t, \sigma_t^2 I) \quad (1)$$

$$p_\theta(x_{t-1} | x_t, \sigma_t, s_t) = \mathcal{N}(x_{t-1}; \mu_\theta(x_t, \sigma_t, s_t), \sigma_t^2 I), \quad (2)$$

exactly mirroring the usual practice of sampling the noise level σ_t uniformly in log-space. Hence the network encounters the full spectrum of noise levels *and* spatial resolutions while seeing each training sample only once.

Embedding every latent back to full resolution with $\tilde{x}_t = U_{s_t}(x_t)$, the hierarchical EDM loss is

$$\mathcal{L}_{\text{H-EDM}}(\theta) = \mathbb{E}_{t, x_0, \epsilon} \left[w(\sigma_t) \left\| \epsilon - f_\theta(\tilde{x}_t + \sigma_t \epsilon, \sigma_t, s_t) \right\|_2^2 \right],$$

where f_θ is the score network and $w(\sigma_t)$ is the usual EDM weighting term.

Because each (h_t, w_t) is sampled once per example, the model learns a coarse-to-fine mapping with no additional passes through the data. Equations 1–2 reduce to the standard EDM when D_{s_t} and U_{s_t} are the identity⁸, ensuring drop-in compatibility with existing code. The formulation matches the visual narrative in the attached figure: blue arrows depict the noise/dimension destruction kernels $q(x_t | x_{t-1})$, while the straight arrows illustrate the learned reverse kernels $p_\theta(x_{t-1} | x_t, \sigma_t, s_t)$.

See the below algorithm outlined for the sampling procedure at training and inference respectively with the below method. Note that steps highlighted in blue are unique to the hierarchical model proposed to enforce a coarse-to-fine generation. exactly mirroring the usual practice of sampling the noise level σ_t uniformly in log-space. Hence the network encounters the full spectrum of noise levels *and* spatial resolutions while seeing each training sample only once.

Embedding every latent back to full resolution with $\tilde{x}_t = U_{s_t}(x_t)$, the hierarchical EDM loss is

$$\mathcal{L}_{\text{H-EDM}}(\theta) = \mathbb{E}_{t, x_0, \epsilon} \left[w(\sigma_t) \left\| \epsilon - f_\theta(\tilde{x}_t + \sigma_t \epsilon, \sigma_t, s_t) \right\|_2^2 \right],$$

⁸In this context, the identity would be if a shape schedule of the full final resolution is used throughout the whole schedule process: $s_t = (x_T, y_T)$ where $t = 1 \dots T$ for each intermediate step

where f_θ is the score network and $w(\sigma_t)$ is the usual EDM weighting term.

Because each (h_t, w_t) is sampled once per example, the model learns a coarse-to-fine mapping with no additional passes through the data. Equations (1)–(2) reduce to the standard EDM when D_{s_t} and U_{s_t} are the identity, ensuring drop-in compatibility with existing code. The formulation matches the visual narrative in the attached figure: blue arrows depict the forward kernels $q(x_t | x_{t-1})$, while the straight arrows illustrate the learned reverse kernels $p_\theta(x_{t-1} | x_t, \sigma_t, s_t)$.

See the below algorithm outlined for the sampling procedure at training and inference respectively with the below method. Note that steps highlighted in blue are unique to the hierarchical model proposed to enforce a coarse-to-fine generation.

Algorithm 1 Training (Hierarchical Forward Process)

Require: dataset $q(x_0)$, noise schedule $\{\sigma_t\}_{t=1}^T$, **shape schedule** $\{(h_t, w_t)\}_{t=1}^T$, network f_θ

- 1: **repeat**
- 2: $x_0 \sim q(x_0)$
- 3: $t \sim \text{Uniform}(\{1, \dots, T\})$
- 4: $\epsilon \sim \mathcal{N}(0, I)$
- 5: $x_t \leftarrow D_t(x_0)$ ▷ down-sample to (h_t, w_t)
- 6: $z \leftarrow \sqrt{\alpha_t} x_t + \sqrt{1 - \alpha_t} \epsilon$
- 7: **gradient step** on $\|\nabla_\theta \epsilon - f_\theta(U_t(z), t, (h_t, w_t))\|_2^2$
- 8: **until** converged

Algorithm 2 Sampling (Hierarchical Reverse Process)

Require: f_θ , noise $\{\sigma_t\}_{t=1}^T$, **shape schedule** $\{(h_t, w_t)\}_{t=1}^T$

- 1: $x_T \sim \mathcal{N}(0, I_{h_T \times w_T})$
- 2: **for** $t = T, \dots, 1$ **do**
- 3: $\tilde{x}_t \leftarrow U_t(x_t)$ ▷ upsample to full res
- 4: $\epsilon_t \leftarrow f_\theta(\tilde{x}_t, t, (h_t, w_t))$
- 5: $x_{t-1} \leftarrow \frac{1}{\sqrt{\alpha_t}} (\tilde{x}_t - \frac{1 - \alpha_t}{\sqrt{1 - \alpha_t}} \epsilon_t)$
- 6: **if** $t > 1$ **then**
- 7: $z \sim \mathcal{N}(0, I)$
- 8: $x_{t-1} \leftarrow x_{t-1} + \sigma_t z$
- 9: $x_{t-1} \leftarrow D_{t-1}(x_{t-1})$ ▷ project to next latent size
- 10: **return** x_0

3.3 Monotone KL decomposition across scales

At its core, downscaling can be framed as an optimal transport problem between the low and high resolution resolved weather distributions [35]. We seek to determine the optimal transformation

Write q_t and p_t for the true and model marginals of x_t in 1–2. Because D_t is information-non-increasing and U_t is a right-inverse in expectation, the *chain rule of relative entropy* yields⁹

$$KL(q_{t-1} \| p_{t-1}) = \underbrace{KL(D_t q_{t-1} \| D_t p_{t-1})}_{\text{coarse divergence}} + E_{x_t \sim q_t} KL(q_{t-1} | x_t \| p_{t-1} | x_t), \quad (3)$$

the second term being always non-negative. 3 shows that *matching the down-sampled marginals can only decrease the fine-scale KL*. Summation over t telescopes:

For the HDD forward–reverse pair 1–2,

$$KL(q_0 \| p_0) = \sum_{t=1}^T \left[KL(D_t q_{t-1} \| D_t p_{t-1}) - KL(D_t q_t \| D_t p_t) \right] \geq 0,$$

and the summand is non-negative for every t . Consequently the coarse-to-fine procedure is *monotonically improving*: each successful fit at scale t tightens an upper bound on the ultimate divergence at full resolution.

Proof. Apply 3 at steps t and $t+1$, subtract, and note that $KL(D_t q_t \| D_t p_t) = KL(q_t \| p_t)$ because D_t is the identity on $\mathbb{R}^{h_t \times w_t \times C}$. Summation over t finishes the argument. \square

Implications. 3.3 justifies a two-phase optimisation strategy: (i) minimise the *coarse* EDM loss (large σ_t , small shape) until $KL(D_t q_{t-1} \| D_t p_{t-1})$ plateaus; (ii) progressively unlock finer scales. Empirically this drastically improves inference time for the similiar RMSE.

⁹A proof appears in Appendix E.

4 What is the Theoretical Speedup?

We seek to define the theoretical improvement in processing speed for different shape schedules at training and inference. Note that as a standard UNET is being used as the underlying architecture, processing time scales linearly with pixels; this would not be the case for an attention-based architecture like ViT but the below calculations could be scaled quadratically in this instance.

Note that this section represents the theoretical upper bound for performance improvement as this varies slightly with the size of image, the number timesteps T and ignores any overhead operations.

Let a clean image be $x_0 \in \mathbb{R}^{H \times W \times C}$ with full area $A = HW$. During training we draw a *single* noise-shape index $t \sim \text{Uniform}\{1, \dots, T\}$ per minibatch and replace the Gaussian-only corruption of EDM with the composite operator $x_{t-1} \mapsto D_{s_t}(x_{t-1} + \sigma_t \varepsilon)$ that *downsamples first, denoises later*. Write $A_t = h_t w_t$ for the area at step t and define the *normalised mean area*

$$\alpha = \frac{1}{T A} \sum_{t=1}^T A_t, \quad \alpha \in (0, 1]. \quad (1)$$

α is the fraction of pixels—relative to baseline EDM—consumed *on average* by one network call; its reciprocal is therefore the ideal pixel/FLOP speed-up:

$$S_{\text{train}} = S_{\text{infer}} = \frac{1}{\alpha}. \quad (2)$$

4.1 Drop-in shape schedulers

(i) Equally Spaced Shrink At each diffusion step we follow a linear ramp from $(1, 1) \rightarrow (H, W)$ in T equal increments:

$$h_t = H - \frac{t-1}{T-1}(H-1), \quad w_t = W - \frac{t-1}{T-1}(W-1).$$

The instantaneous area therefore decays quadratically, $A_t = h_t w_t = \left(1 - \frac{t-1}{T-1}\right)^2 A$. Averaging over the schedule gives the dimension-agnostic mean area

$$\alpha_{\text{lin}} = \frac{1}{T A} \sum_{t=1}^T A_t = \frac{1}{T} \sum_{k=0}^{T-1} \left(1 - \frac{k}{T-1}\right)^2 = \frac{1}{3}.$$

Via the general rule $S = 1/\alpha$ this implies a tight $\boxed{3 \times}$ pixel- and FLOP-saving ceiling, drop-in for vanilla EDM.

(ii) Unit-shrink per denoise step. At every diffusion step *both* spatial dimensions drop by a single pixel until reaching one:

$$h_t = \max(1, H - (t-1)), \quad w_t = \max(1, W - (t-1)).$$

For $T \leq \min(H, W)$ no clamping is active, giving

$$\sum_{t=1}^T A_t = T H W - \frac{(T-1)T}{2} (H+W) + \frac{(T-1)T(2T-1)}{6}.$$

Plugging this sum into (1)–(2) yields the closed-form

$$S_{\text{unit}} = \left[1 - \frac{(T-1)}{2A} (H+W) + \frac{(T-1)(2T-1)}{6A} \right]^{-1}.$$

Example. $H=144, W=272, T=50$: $\alpha \approx 0.760 \Rightarrow S \approx 1.32 \times$.

4.2 Summary of theoretical pixel savings

Shape scheduler	α	Speed-up $S = 1/\alpha$
Linear shrink $(h_t, w_t) \propto 1 - \frac{t-1}{T-1}$	$\frac{1}{3}$	$3\times$
Unit-shrink $(h_t, w_t) = (H - (t-1), W - (t-1))$	see Eq. (3)	$\approx 1.32\times$ (50 steps)

All schedules are *drop-in*: when $D_{s_t} = U_{s_t} = I$ they revert to vanilla EDM. Eq. (2) therefore gives an upper-bound on pixel, FLOP and memory savings obtainable with the HDD framework. We note that this is a higher speed up than comparable image-based approaches due to the choice of shape scheduler [38].

5 Experiments

5.1 ERA5 Experiment

We trained a model on 29 years of ERA5 reanalysis data across temperature, u/v component of wind and precipitation from 1990 to 2019 over the Australian domain¹⁰. The task was to downscale the resolution from 1.5° to 0.25°. This was trained for 144 hours on two A100 GPUs for 360 epochs. Training time/resources were mimicked for Earth-ViT and the base EDM and all models achieved convergence¹¹. We then evaluate each of these models on the same task for five years of ERA5 data from January 2020 to December 2024.

See appendix E for further information on sampling procedures and ablations on metrics. Note that Earth-ViT is based on the popular weather forecasting model *panguweather* with several slight modifications for the downscaling setting. See [7] for further information on Earth-ViT and Appendix E for information on the training procedure for this setting.

Table 1: Performance for various models trained on the ERA5 task over Australia. Although the direct comparison is not included here, we note that the ‘Base EDM’ model is the same as the backbone for popular downscaling model Corrdiff from NVIDIA [23, 17]. We motivate the inclusion of these shape schedules in the below ablation

Model	RMSE	PSNR
Bilinear Interpolation	0.362755	9.54
Earth-ViT (Finetuned PanguWeather [7])	0.317410	10.63
Base EDM – 50 Steps	0.000197	29.17
EDM – Hierarchical – 50 steps – Equally Spaced	0.000158	31.38
EDM – Hierarchical – 50 steps – 3 denoise steps per shape step	0.000157	31.40
EDM – Hierarchical – 500 steps – Equally Spaced	0.000132	33.19
EDM – Hierarchical – 500 steps – 3 denoise steps per shape step	0.000131	33.27

5.2 Ablation results - Hierarchical Scheduler

We now take the trained HDD model and examine the effect of different shape schedules to validate at what frequency we should be increasing dimensions vs just denoising. Note that we take the best model on the ERA5 task (HDD - Hierarchical - 500 steps) and apply it below with different shape schedules. There is an expected tradeoff between the the total intermediate number of pixels processed at inference and RMSE. However, it is interesting to note that the the most extreme model with equally spaced dimension jumps between (1,1) and (144,272) still retains very similar results to the base case. We conclude that the additional shape information being passed to them model allows it to process the coarse details just as in a normal diffusion model, but at a fraction of the inference cost.

¹⁰Over a latitude/longitude bounding box of (-7.75,109) to (-43.5,176.75)

¹¹See appendix E for further training/sampling information

Table 2: Same task as in section 5.1 but with differing shape schedules ablated

Model	RMSE	PSNR
Equally Spaced Steps	0.000131	33.262
Move in tandem – 1 denoise step per shape step	0.000129	33.40
2 denoise steps per shape step	0.000129	33.36
3 denoise steps per shape step	0.000129	33.34
50 denoise steps per shape step	0.000131	33.21
500 denoise steps per shape step	0.000133	33.11

Interestingly, enforcing a slight coarse to fine generation with minimal overall pixel loss appears to yield the best results. However, Different shape schedules show that increasing the denoising steps per shape (visualised in 3 as the flattening slope) leads to an initial improvement before leveling out. The final ablation ‘500 denoise steps per shape step’ is equivalent to having no dimension reducing steps but still performs much better than the base model in section 5.1.

5.3 GCM Application and comparison to Nested RCM Results

We then take the models trained on the ERA5 task and apply these on data generated from general circulation models (GCMs). The GCM data is available at the very coarse resolution of approximately 1.5° grids due to the aforementioned computational constraints with generating this data¹³. Data is then downsampled to a 0.25° resolution over Australia and evaluated against precipitation data from the Australian Gridded Climate Dataset (AGCD).

We compute results against a variety of established precipitation-specific climate evaluation metrics [15]. We note that both models pass 6/6 evaluation criteria benchmarks for accuracy metrics and report some of these metrics in the table below. See results for the CNRM-CERFACS GCM below; results for additional GCMs are reported in appendix D¹⁴. Figure 4 shows the opportunity of developing a single foundation model that could be applied on a whole spectrum of GCMs to get the full spectrum of climate outcomes; something which is currently underrepresented with only 2/5 SSP IPCC pathways downsampled; representing only a narrow portion of the potential future outcomes[28].

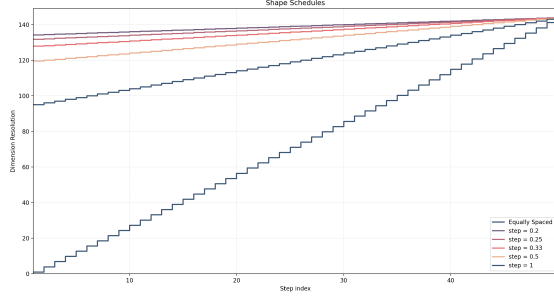


Figure 3: The dimensions of the downsampled image as it evolves with the number of steps. Note that in the extreme case where we equally our dimension jumps over the steps, we only process one third as many pixels at inference - see section four for further breakdown on this.

Table 3: Relevant climate metrics SCorr, MAPE from [15] and Computational Efficiency for CNRM-CERFACS-driven downscaling runs

Model	SCorr	MAPE	kgCO ₂ Emitted
HDD	0.79	0.51	53kg Training + 3kg ¹⁵ inference
Base EDM	0.78	0.22	105kg Training + 5kg inference
CCAM-1704	0.89	0.26	1032kg
Earth-ViT	0.80	0.31	51kg Training + 2kg

¹²This equates to grids of approximately 167km x 167km

¹³See appendix D for further information

¹⁴See also appendix D for the full suite of climate evaluation metrics

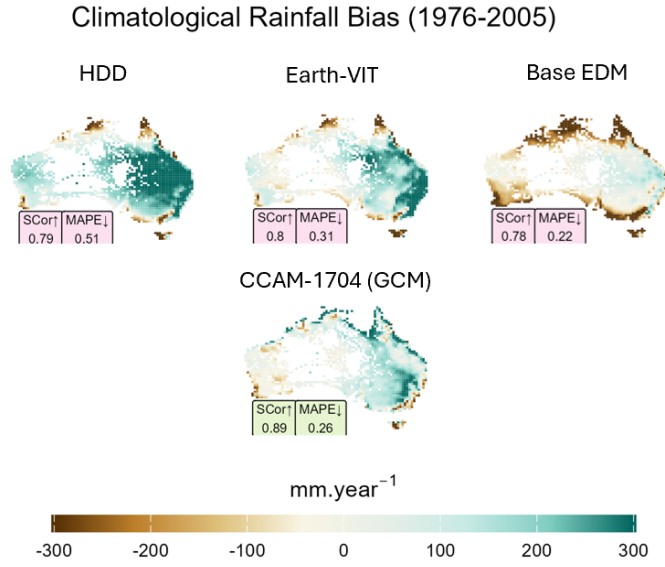


Figure 4: AI models cover the full spectrum of wet/dry climate outcomes.

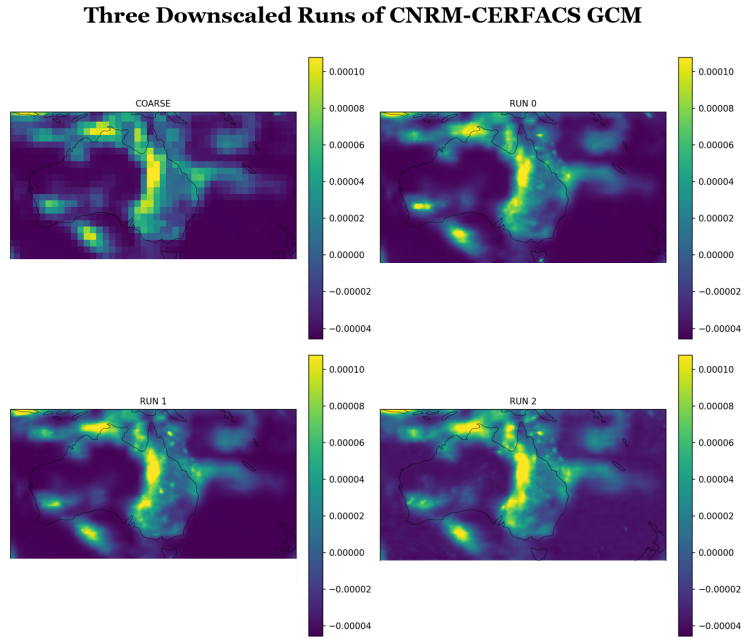


Figure 5: Model applied over the Australian extent of the CNRM-CERFACS General Circulation model

6 Conclusion

HDD shows that a coarse-to-fine ladder inside a diffusion model is enough to cut the pixel budget—and therefore the FLOPs and CO₂—by roughly two-thirds while preserving most of the accuracy on ERA5 and multiple CMIP6 GCMs. The result is high-resolution climate data at a fraction of the computational and monetary cost of both dynamical nests and standard diffusion models. This can be applied to any existing diffusion architecture with the same process as described in section 3, but note

that it requires retraining the existing diffusion model to incorporate two additional scalars. In the future, such a model could be used to downscale the full distribution of potential climate outcomes. The societal impact of this work is nuanced, improved climate projections are inherently important for understanding our changing climate; yet, there is the potential for increasing insurance premiums in at-risk areas.

6.1 Limitations

Although the results indicate that HDD performs well on the ERA5 use-case, when applied zero-shot on the GCM task, the conclusion is less clear. The HDD model beats the dynamical model and base diffusion model on some metrics, but performs worse on others. We also note that although the model structure only requires an additional 2 scalars of input over any base diffusion model¹⁶, it still needs to be retrained to be added to an existing model. We also do not test on future data¹⁷.

7 Acknowledgements

The work was undertaken using resources from the National Computational Infrastructure (NCI), which is supported by the Australian Government. SH acknowledges the support of the Australian Research Council Centre of Excellence for the Weather of the 21st Century (CE230100012).

References

- [1] *A National Strategy for Advancing Climate Modeling*. National Academies Press, December 2012.
- [2] V. Balaji, Fleur Couvreur, Julie Deshayes, Jacques Gautrais, Frédéric Hourdin, and Catherine Rio. Are general circulation models obsolete? *Proceedings of the National Academy of Sciences*, 119(47), November 2022.
- [3] Kaifeng Bi, Lingxi Xie, Hengheng Zhang, Xin Chen, Xiaotao Gu, and Qi Tian. Pangu-weather: A 3d high-resolution model for fast and accurate global weather forecast, 2022.
- [4] Andrew Campbell, William Harvey, Christian Weillbach, Valentin De Bortoli, Tom Rainforth, and Arnaud Doucet. Trans-dimensional generative modeling via jump diffusion models, 2023.
- [5] Sixiang Chen, Jinbin Bai, Zhuoran Zhao, Tian Ye, Qingyu Shi, Donghao Zhou, Wenhao Chai, Xin Lin, Jianzong Wu, Chao Tang, Shilin Xu, Tao Zhang, Haobo Yuan, Yikang Zhou, Wei Chow, Linfeng Li, Xiangtai Li, Lei Zhu, and Lu Qi. An empirical study of gpt-4o image generation capabilities, 2025.
- [6] Thomas M. Cover and Joy A. Thomas. *Elements of Information Theory*. Wiley, April 2005.
- [7] Declan Curran, Hira Saleem, Sanaa Hobeichi, and Flora Salim. Resolution-agnostic transformer-based climate downscaling, 2024.
- [8] Declan Curran, Hira Saleem, and Flora Salim. Identifying high resolution benchmark data needs and novel data-driven methodologies for climate downscaling, 2024.
- [9] Sandar Dielman. Diffusion is spectral autoregression. <https://sander.ai/2024/09/02/spectral-autoregression.html>, 2024.
- [10] D. D’Onofrio, E. Palazzi, J. von Hardenberg, A. Provenzale, and S. Calmanti. Stochastic rainfall downscaling of climate models. *Journal of Hydrometeorology*, 15(2):830–843, April 2014.
- [11] K. S. Gage and G. D. Nastrom. Theoretical interpretation of atmospheric wavenumber spectra of wind and temperature observed by commercial aircraft during gasp. *Journal of the Atmospheric Sciences*, 43(7):729–740, April 1986.

¹⁶One scalar for each of the (h_t, w_t) shapes in s_t

¹⁷Lack of ground truth makes this difficult in addition to shifting climate distribution

- [12] Eleftherios Gkioulekas and Ka-Kit Tung. Recent developments in understanding two-dimensional turbulence and the nastrom–gage spectrum. *Journal of Low Temperature Physics*, 145(1–4):25–57, December 2006.
- [13] Jonathan Ho, Ajay Jain, and Pieter Abbeel. Denoising diffusion probabilistic models. *Advances in neural information processing systems*, 33:6840–6851, 2020.
- [14] Aapo Hyvärinen, Jarmo Hurri, and Patrik O. Hoyer. *Natural Image Statistics*. Springer London, 2009.
- [15] Rachael N. Isphording, Lisa V. Alexander, Margot Bador, Donna Green, Jason P. Evans, and Scott Wales. A standardized benchmarking framework to assess downscaled precipitation simulations. *Journal of Climate*, 37(4):1089–1110, February 2024.
- [16] Yang Jin, Zhicheng Sun, Ningyuan Li, Kun Xu, Kun Xu, Hao Jiang, Nan Zhuang, Quzhe Huang, Yang Song, Yadong Mu, and Zhouchen Lin. Pyramidal flow matching for efficient video generative modeling, 2024.
- [17] Tero Karras, Miika Aittala, Timo Aila, and Samuli Laine. Elucidating the design space of diffusion-based generative models, 2022.
- [18] Louise Kauffmann, Stephen RamanoÅ«l, and Carole Peyrin. The neural bases of spatial frequency processing during scene perception. *Frontiers in Integrative Neuroscience*, 8, May 2014.
- [19] Peter E. Kloeden and Eckhard Platen. *Numerical Solution of Stochastic Differential Equations*. Springer Berlin Heidelberg, 1992.
- [20] Dmitrii Kochkov, Janni Yuval, Ian Langmore, Peter Norgaard, Jamie Smith, Griffin Mooers, Milan Klöwer, James Lottes, Stephan Rasp, Peter Düben, Sam Hatfield, Peter Battaglia, Alvaro Sanchez-Gonzalez, Matthew Willson, Michael P. Brenner, and Stephan Hoyer. Neural general circulation models for weather and climate. *Nature*, 632(8027):1060–1066, July 2024.
- [21] S. Kullback and R. A. Leibler. On information and sufficiency. *The Annals of Mathematical Statistics*, 22(1):79–86, March 1951.
- [22] Remi Lam, Alvaro Sanchez-Gonzalez, Matthew Willson, Peter Wirsberger, Meire Fortunato, Ferran Alet, Suman Ravuri, Timo Ewalds, Zach Eaton-Rosen, Weihua Hu, Alexander Merose, Stephan Hoyer, George Holland, Oriol Vinyals, Jacklynn Stott, Alexander Pritzel, Shakir Mohamed, and Peter Battaglia. Graphcast: Learning skillful medium-range global weather forecasting, 2022.
- [23] Morteza Mardani, Noah Brenowitz, Yair Cohen, Jaideep Pathak, Chieh-Yu Chen, Cheng-Chin Liu, Arash Vahdat, Mohammad Amin Nabian, Tao Ge, Akshay Subramaniam, Karthik Kashinath, Jan Kautz, and Mike Pritchard. Residual corrective diffusion modeling for km-scale atmospheric downscaling, 2023.
- [24] David Navon. Forest before trees: The precedence of global features in visual perception. *Cognitive Psychology*, 9(3):353–383, July 1977.
- [25] Aude Oliva and Antonio Torralba. *Chapter 2 Building the gist of a scene: the role of global image features in recognition*, page 23–36. Elsevier, 2006.
- [26] Neelesh Rampal, Sanaa Hobeichi, Peter B. Gibson, Jorge Baño-Medina, Gab Abramowitz, Tom Beucler, Jose González-Abad, William Chapman, Paula Harder, and José Manuel Gutiérrez. Enhancing regional climate downscaling through advances in machine learning. *Artificial Intelligence for the Earth Systems*, 3(2), April 2024.
- [27] Nicola Rebora, Luca Ferraris, Jost von Hardenberg, and Antonello Provenzale. Rainfarm: Rain-fall downscaling by a filtered autoregressive model. *Journal of Hydrometeorology*, 7(4):724–738, August 2006.

- [28] Keywan Riahi, Detlef P. van Vuuren, Elmar Kriegler, Jae Edmonds, Brian C. O'Neill, Shinichiro Fujimori, Nico Bauer, Katherine Calvin, Rob Dellink, Oliver Fricko, Wolfgang Lutz, Alexander Popp, Jesus Crespo Cuaresma, Samir KC, Marian Leimbach, Leiwen Jiang, Tom Kram, Shilpa Rao, Johannes Emmerling, Kristie Ebi, Tomoko Hasegawa, Petr Havlik, Florian Humpenöder, Lara Aleluia Da Silva, Steve Smith, Elke Stehfest, Valentina Bosetti, Jiyong Eom, David Gernaat, Toshihiko Masui, Joeri Rogelj, Jessica Streffer, Laurent Drouet, Volker Krey, Gunnar Luderer, Mathijs Harmsen, Kiyoshi Takahashi, Lavinia Baumstark, Jonathan C. Doelman, Mikiko Kainuma, Zbigniew Klimont, Giacomo Marangoni, Hermann Lotze-Campen, Michael Obersteiner, Andrzej Tabeau, and Massimo Tavoni. The shared socioeconomic pathways and their energy, land use, and greenhouse gas emissions implications: An overview. *Global Environmental Change*, 42:153–168, January 2017.
- [29] Severi Rissanen, Markus Heinonen, and Arno Solin. Generative modelling with inverse heat dissipation, 2022.
- [30] H.L. Royden and P. Fitzpatrick. *Real Analysis*. Prentice Hall, 2010.
- [31] Walter Rudin. *Real and complex analysis, 3rd ed.* McGraw-Hill, Inc., USA, 1987.
- [32] Yang Song, Jascha Sohl-Dickstein, Diederik P. Kingma, Abhishek Kumar, Stefano Ermon, and Ben Poole. Score-based generative modeling through stochastic differential equations, 2020.
- [33] Keyu Tian, Yi Jiang, Zehuan Yuan, Bingyue Peng, and Liwei Wang. Visual autoregressive modeling: Scalable image generation via next-scale prediction. 2024.
- [34] A. van der Schaaf and J.H. van Hateren. Modelling the power spectra of natural images: Statistics and information. *Vision Research*, 36(17):2759–2770, September 1996.
- [35] Zhong Yi Wan, Ricardo Baptista, Yi-fan Chen, John Anderson, Anudhyan Boral, Fei Sha, and Leonardo Zepeda-Núñez. Debias coarsely, sample conditionally: Statistical downscaling through optimal transport and probabilistic diffusion models, 2023.
- [36] Robbie A. Watt and Laura A. Mansfield. Generative diffusion-based downscaling for climate, 2024.
- [37] Matteo Willeit, Roberta Amorati, Andrea Montani, Valentina Pavan, and Maria Stefania Tesini. Comparison of spectral characteristics of precipitation from radar estimates and cosmo-model predicted fields. *Meteorology and Atmospheric Physics*, 127(2):191–203, November 2014.
- [38] Han Zhang, Ruili Feng, Zhantao Yang, Lianghua Huang, Yu Liu, Yifei Zhang, Yujun Shen, Deli Zhao, Jingren Zhou, and Fan Cheng. Dimensionality-varying diffusion process, 2022.

A Radially-Averaged Power-Spectral Density (RAPSD)

Figures 1 and 2 in the main text visualise how power is redistributed when an ERA5 field is either (i) coarsened by repeated $2\times$ down-sampling or (ii) contaminated with Gaussian noise of increasing variance. This appendix formalises the metrics that underlie those plots and derives the theoretical curves that explain their shapes.

A.1 From a 2-D field to a 1-D spectrum

Let the clean field be a real-valued array $x \in \mathbb{R}^{N_y \times N_x}$, indexed by pixel coordinates $\mathbf{r} = (n, m)$. Its discrete Fourier transform (DFT) is

$$X(\mathbf{k}) = \mathcal{F}\{x\}(\mathbf{k}) = \sum_{n=0}^{N_y-1} \sum_{m=0}^{N_x-1} x_{n,m} e^{-2\pi i (k_y n/N_y + k_x m/N_x)}, \quad \mathbf{k} = (k_x, k_y). \quad (4)$$

The *power-spectral density* (PSD) is the squared magnitude $P(\mathbf{k}) = |X(\mathbf{k})|^2$. For many geophysical or photographic images the statistics are approximately isotropic, so it is convenient to collapse the 2-D PSD into a 1-D function of radius $f = \|\mathbf{k}\|$ (spatial frequency):

$$\text{RAPSD}(f_j) = \frac{1}{|\mathcal{A}_j|} \sum_{\mathbf{k} \in \mathcal{A}_j} P(\mathbf{k}), \quad \mathcal{A}_j = \{\mathbf{k} : f_j \leq \|\mathbf{k}\| < f_{j+1}\}, \quad (5)$$

where the annuli $\{\mathcal{A}_j\}_{j=0}^{J-1}$ partition the Fourier plane into logarithmically-spaced bins ($f_{j+1}/f_j = \text{const}$). Log-log plots of $f \mapsto \text{RAPSD}(f)$ often reveal the empirical power law $\text{RAPSD}(f) \propto f^{-\alpha}$ with $\alpha \approx 2$ for natural images and for many meteorological fields (e.g. the Nastrom–Gage kinetic-energy spectrum).

A.2 Effect of 2 x spatial down-sampling

Down-sampling by an integer factor s reduces the Nyquist frequency from $f_{\max} = 1/2$ (in pixel units) to f_{\max}/s . Assuming ideal low-pass pre-filtering, all energy above f_{\max}/s is discarded; below that limit the PSD is merely scaled by s^2 to conserve total variance. For five binary-decade reductions $s \in \{2, 4, 8, 16, 32\}$ (as in **Fig. 1**) one expects

$$\text{RAPSD}_s(f) = \begin{cases} s^2 \text{RAPSD}_{\text{orig}}(f), & f < \frac{1}{2s}, \\ 0, & f \geq \frac{1}{2s}. \end{cases}$$

Hence the curves in Fig. 1 coincide at low f and peel off successively at their (progressively smaller) Nyquist cut-offs—exactly the trend observed.

A.3 Effect of additive white noise

Let $\varepsilon \sim \mathcal{N}(0, \sigma_n^2)$ be i.i.d. pixel noise. Because the DFT is linear and because white noise is spectrally flat,

$$Y = X + \varepsilon, \quad (6)$$

$$\mathbb{E}[P_Y(\mathbf{k})] = P_X(\mathbf{k}) + \sigma_n^2, \quad (7)$$

so every RAPSD curve is translated upward by the *same* constant σ_n^2 . Define the *hinge frequency* $f^*(\sigma_n) = \min\{f : \text{RAPSD}_X(f) \leq \sigma_n^2\}$. For $f < f^*$ the spectrum is signal-dominated and remains unchanged; for $f > f^*$ the spectrum is noise-dominated and becomes flat at the level σ_n^2 . Because the notebook sets $\sigma_n = \text{noise_factor} \times \sigma_X$, the plateau height scales quadratically with the chosen `noise_factor`. The five coloured curves of **Fig. 2** therefore realise

$$\text{RAPSD}_{\text{noise}}(f | \lambda) = \text{RAPSD}_X(f) + \lambda^2 \sigma_X^2, \quad \lambda \in \{0, 0.25, 0.5, 0.75, 1.0\}.$$

Each ten-fold rise in λ^2 shifts the horizontal tail up by the same factor and pushes f^* leftward, reducing the bandwidth in which the underlying flow field is recoverable.

A.4 Relevance for coarse-to-fine diffusion scheduling

In a Gaussian diffusion process the state at noise level σ_t is $x_t = \alpha_t x_0 + \sigma_t \varepsilon$ (with $\varepsilon \sim \mathcal{N}(0, 1)$). Because RAPSD adds linearly, low frequencies re-emerge first as σ_t decays, while high-frequency detail appears only when $\sigma_t^2 \lesssim \text{RAPSD}_X(f)$. Thus the reverse-time sampler automatically follows a coarse-to-fine trajectory in spectral space. The patterns in Figures 1 and 2 therefore provide the mathematical justification for conditioning a diffusion model either on a sequence of coarsened resolutions or on a carefully curated noise schedule when generating meteorological fields.

B Coarse-to-Fine Diffusion Approximates the Score Function on Simpler Distributions

Recall that in standard diffusion models, the *score function* at time t is

$$\nabla_x \log p_t(x),$$

which describes the gradient of the log-density for a progressively noisier version of x_0 . Learning the reverse process is equivalent to learning to denoise (or equivalently approximate this score) at various noise levels.

Coarse Distributions as Simpler Targets. When the image is downsampled to coarser resolutions (fewer pixels, fewer degrees of freedom), the induced data distribution

$$p_{\text{coarse}}(x) = \text{distribution of downsampled images}$$

is generally “simpler” to model. Intuitively, high-frequency details are removed, so spatial correlations are more tractable, and the manifold of coarse-resolution images is lower-dimensional. Consequently, predicting the score

$$\nabla_x \log p_{\text{coarse}}(x)$$

becomes easier: there are fewer fine-grained features to learn, and the model focuses on broad, low-frequency structure.

Hierarchical vs. Single-Scale Approach. By first learning to approximate the score at a coarse distribution,

$$s_t^{(\text{coarse})}(x) \approx \nabla_x \log p_{\text{coarse},t}(x),$$

the model handles an easier inverse problem. Then, as the resolution is gradually increased, each subsequent diffusion (and corresponding score function) refines the result:

$$s_t^{(\text{finer})}(x) \approx \nabla_x \log p_{\text{finer},t}(x).$$

Each finer scale deals with distributions that are “closer” to the full-resolution distribution but still easier than jumping directly from pure noise to a full-resolution image in one step.

Connection to Score-Based Diffusion. In the continuous SDE view, we can think of downsampling as reducing the dimensionality or bandwidth of the data, so at time t , the *score* $\nabla_x \log p_t(x)$ lives on a simpler manifold. Discretizing this idea across multiple resolutions amounts to learning a sequence of denoising (or score) functions:

$$f_\theta(\mathcal{U}(x_t), t) \approx \nabla_x \log p_{\text{downsampled},t}(x),$$

where $\mathcal{U}(x_t)$ is an upsampled version of x_t . Such a hierarchical approach effectively breaks a complex score-estimation problem into stages where each stage handles a simpler, coarser distribution; with each increase in resolution progressively conditioning on the previous result. The autoregressive coarse to fine nature of this generation is intuitive—as previously discussed, humans understand images in a coarse to fine manner with

Summary. Hence, this method approximates the score function on these coarser distributions—where the image space is significantly reduced in size and complexity—before progressively shifting to higher resolutions. This *coarse-to-fine* strategy stabilizes training and provides a more direct way for the network to focus first on large-scale structure and then on finer details, thus approximating the score function in a stepwise manner from simpler (coarse) to more complex (full-resolution) distributions.

C Why Increasing the Number of Dimension-Destruction Steps Improves Results

C.1 Discretizing a Continuous Diffusion Process in Time

A powerful perspective, introduced in [32], is to view diffusion models as discretized solutions to a *continuous-time* Stochastic Differential Equation (SDE). For standard DDPM [13] (without dimension destruction), the forward (noising) process in continuous time can be written as:

$$d\mathbf{x} = f(\mathbf{x}, t) dt + g(t) d\mathbf{w}, \quad (8)$$

where \mathbf{w} is a standard Wiener process (Brownian motion) and $t \in [0, 1]$. Conceptually, $f(\mathbf{x}, t)$ and $g(t)$ define the drift and diffusion coefficients that gradually corrupt data into noise.

Reverse-Time SDE. By reversing the time variable from $t = 1$ down to $t = 0$, one obtains the *reverse* SDE:

$$d\mathbf{x} = \left[f(\mathbf{x}, t) - g(t)^2 \nabla_{\mathbf{x}} \log p_t(\mathbf{x}) \right] dt + g(t) d\bar{\mathbf{w}}, \quad (9)$$

where $p_t(\mathbf{x})$ is the (instantaneous) distribution of \mathbf{x} at time t , and $\bar{\mathbf{w}}$ is a Brownian motion in reverse time. This reverse SDE perfectly “denoises” the corrupted data back to a clean sample as t goes from 1 down to 0.

Discrete Approximation via Euler–Maruyama. In practice, we discretize the interval $[0, 1]$ into N steps, $t_1 < t_2 < \dots < t_N$, and approximate the update with an explicit numerical scheme (e.g., Euler–Maruyama):

$$\mathbf{x}_{t_{k-1}} \approx \mathbf{x}_{t_k} + \left[f(\mathbf{x}_{t_k}, t_k) - g(t_k)^2 \nabla_{\mathbf{x}} \log p_{t_k}(\mathbf{x}_{t_k}) \right] \Delta t + g(t_k) \sqrt{\Delta t} \boldsymbol{\eta}_k,$$

where $\Delta t = t_{k-1} - t_k$ is small, and $\boldsymbol{\eta}_k \sim \mathcal{N}(0, \mathbf{I})$. The fewer steps N we use, the *larger* each Δt —and hence the larger the local approximation error at each step.

Key Point (Time Discretization). As $N \rightarrow \infty$, $\Delta t \rightarrow 0$, and the discrete chain converges to the exact solution of the SDE. Therefore, *more steps* \implies *smaller local errors* \implies *better final reconstruction*. Empirically, one observes that generating samples with more reverse steps (e.g., 1000 steps vs. 50) yields sharper images, because smaller increments in each denoising step incur fewer approximation artifacts [13].

C.2 Accumulation of Local Errors

Each discrete reverse step $p_\theta(\mathbf{x}_{t-1} | \mathbf{x}_t)$ can introduce some mismatch (e.g. KL divergence) compared to the true $q(\mathbf{x}_{t-1} | \mathbf{x}_t)$. If a single step has a small per-step error ε , over N steps the total discrepancy might accumulate on the order of $O(N \cdot \varepsilon)$. However, when we *increase* N , the per-step error ε often *decreases* because each denoising increment is smaller.

This can be made rigorous by considering the continuum limit $N \rightarrow \infty$, where $\Delta t = 1/N$. Classical SDE analysis (see [19]) shows that under certain regularity conditions, the global approximation error converges to zero as $\Delta t \rightarrow 0$. Thus,

$$\lim_{N \rightarrow \infty} p_\theta(\mathbf{x}_0) = q(\mathbf{x}_0),$$

meaning the learned model recovers the true data distribution in the idealized infinite-step regime (assuming perfect training).

C.3 Dimension-Destruction Viewpoint (Coarse-to-Fine)

In the hierarchical shape-conditioning setting, we introduce a *second axis* of discretization: not only do we add noise at each step, but we also *downsample* (i.e. reduce the spatial resolution). Let us denote the forward dimension-destruction step at time index k as

$$x_k = \mathcal{D}_k(x_{k-1} + \epsilon_k), \quad \epsilon_k \sim \mathcal{N}(0, \sigma_k^2 \mathbf{I}), \quad (10)$$

where \mathcal{D}_k maps $(h_{k-1} \times w_{k-1})$ pixels to $(h_k \times w_k)$ pixels, typically $h_k < h_{k-1}$ and $w_k < w_{k-1}$. The reverse process then *upsamples* to full resolution before denoising. In effect, we are discretizing both (a) the *time* variable **and** (b) the *spatial dimension*.

Finer Discretisation in Dimension. When dimension changes are large (e.g. $64 \times 64 \rightarrow 4 \times 4$ in a single step), the model loses significant high-frequency content all at once, and the reverse step must hallucinate many details in one jump. This is akin to having a large Δt in the SDE sense; the local error can be large and difficult to reverse.

Conversely, if we *split* that dimension change into multiple steps

$$(64 \times 64) \rightarrow (32 \times 32) \rightarrow (16 \times 16) \rightarrow (8 \times 8) \rightarrow (4 \times 4),$$

each step is a smaller “destruction” of high frequencies and structure, so the reverse upsampling + denoising is more accurate (less local error). By increasing the number of dimension-destruction steps, we make these changes more gradual, pushing the discrete approximation closer to the (hypothetical) continuous limit in scale space:

$$\Delta(\text{dimension}) \rightarrow 0.$$

Hence, *more dimension-destruction steps* is exactly parallel to *more time steps* in standard DDPM: it yields finer increments, lower local error, and a more faithful final reconstruction.

C.4 Conclusion: A Double Discretization Argument

Overall, we have two types of discretization:

- **Noise-Level Discretization:** Splitting the time interval $[0, 1]$ into small Δt ’s (as in standard diffusion).
- **Dimension Discretization:** Splitting the resolution reduction into many smaller downsampling increments.

Both can be justified under the same SDE-based argument: *smaller steps in each dimension of transformation* \implies *lower approximation error per step* \implies *better overall fidelity*. Empirical evidence (Tables in Section 5) corroborates that increasing either (or both) the number of time steps and dimension steps significantly improves generation quality metrics such as PSNR, SSIM, and FID

D Climate Benchmark Metrics

This appendix concisely defines the minimum-standard metrics proposed by [15] and adopted in the present study to assess the ability of ML models to capture three fundamental characteristics of rainfall: *How much does it rain?* *Where does it rain?*, and *When does it rain?* The metrics used to quantify these characteristics are listed in Table 2 below. Each metric is accompanied by (i) its mathematical formulation as implemented in our analysis code, (ii) the numerical benchmark that constitutes a ‘pass’, and (iii) a brief explanation of what the metric tells us from a climate science perspective. Where relevant, n denotes the number of non-missing land grid-cells after the AGCD quality mask is applied and w_i the cosine-latitudinal area-weight for cell i . P_i and O_i are the predicted and observed climatological-mean annual rainfall total respectively. We also apply these metrics to evaluate three dynamically downscaled precipitation simulations produced CNRM-CM5 CCAM-1704, HadGEM2-ES RegCM4-7, and MIROC5 CCAM-1704. These datasets are part of the CORDEX-CMIP5 ensemble over the Australasian domain.

D.1 Mean Absolute Percentage Error (MAPE) - How much does it rain?

$$\text{MAPE} = \frac{1}{W} \sum_{i=1}^n w_i \left| \frac{P_i - O_i}{O_i} \right|, \quad W := \sum_{i=1}^n w_i. \quad (11)$$

Benchmark: $\text{MAPE} \leq 0.75$.

Climate meaning. MAPE gauges the proportional bias in climatological mean annual rainfall: values ≤ 0.75 require simulations to be, on average, within 75% of observations—a pragmatic trade-off between model realism and current skill levels.

Table 4: Downscaling performance metrics and estimated carbon footprint for machine-learning (ML) and dynamical-downscaling (DD) configurations over Australia (1976–2005). Results for both HDD and the base EDM were both performed using 50 inference steps and 3 denoise steps per shape step for the HDD models

Driving GCM	Model / RCM	NRMSE	MAD	SCorr	MAPE	kgCO ₂ Train ¹⁸
MIROC5	HDD	0.45	1.0865	0.85	1.1752	~53 kg
CNRM-CM5	HDD	0.62	1.3897	0.79	0.5185	~53 kg
MIROC5	Base EDM	0.54	1.2961	0.81	0.5505	~105 kg
CNRM-CM5	Base EDM	0.56	1.2654	0.78	0.2481	~105 kg
CNRM-CM5	Earth-ViT	0.50	1.1044	0.80	0.3498	~51 kg
CNRM-CM5	CCAM-1704	0.68	0.8698	0.89	0.2600	1032 kg (total)
HadGEM2-ES	RegCM4-7	1.47	1.1586	0.90	1.0223	588 kg (total)
MIROC5	CCAM-1704	0.78	1.1083	0.88	0.3374	Not Available

Table 5: Minimum-standard rainfall metrics (adapted from [15]). Metrics are computed from area-weighted average total rainfall over Australia using the AGCD observational dataset. Amplitude is the difference between maximum and mean monthly rainfall; phase is the month of maximum rainfall.

Fundamental rainfall characteristic	Quantifying metric	Benchmark threshold
How much does it rain?	Mean absolute percentage error (MAPE)	MAPE \leq 0.75
Where does it rain?	Spatial correlation (SCor)	SCor \geq 0.7
When does it rain?	<i>Amplitude</i> : normalised root mean squared error (NRMSE) <i>Phase</i> : mean absolute deviation (MAD; months) of the maximum-rainfall month	<i>Amplitude</i> : NRMSE \leq 0.6 <i>Phase</i> : MAD \leq 2

D.2 Spatial Correlation (SCor) - (Where does it rain?)

$$\text{SCor} = \frac{\sum_{i=1}^n w_i (P_i - \hat{P})(O_i - \hat{O})}{\sqrt{\sum_{i=1}^n w_i (P_i - \hat{P})^2} \sqrt{\sum_{i=1}^n w_i (O_i - \hat{O})^2}}, \quad \hat{P} := \frac{1}{W} \sum_{i=1}^n w_i P_i, \quad \hat{O} := \frac{1}{W} \sum_{i=1}^n w_i O_i. \quad (12)$$

where \hat{P} and \hat{O} are the area-weighted spatial means of P_i and O_i .

Benchmark: SCor \geq 0.7.

Climate meaning. SCor evaluates how well the model reproduces the *spatial pattern* of mean annual rainfall. correlations (\geq 0.7) imply that regional wet and dry zones are captured in the right places, even if the absolute totals differ.

D.3 Seasonal-cycle metrics (When does it rain?)

We define the grid-cell seasonal amplitude A_i , where $A_i = P_i^{\max} - \bar{P}_i$, and M_i as the phase (month index) of that maximum P_i^{\max} . The Normalised RMSE of amplitudes:

$$\text{NRMSE} = \frac{\sqrt{\frac{1}{W} \sum_i w_i (A_i^{\text{mod}} - A_i^{\text{obs}})^2}}{\frac{1}{W} \sum_i w_i A_i^{\text{obs}^2}} \quad (13)$$

where A_i^{mod} and A_i^{obs} are the amplitudes of the prediction and observation respectively.

Benchmark: NRMSE \leq 0.60.

$$\text{MAD} = \frac{1}{W} \sum_{i=1}^n w_i |\Delta\phi(M_i^{\text{mod}}, M_i^{\text{obs}})| \quad (14)$$

where $\Delta\phi$ is the shortest circular distance on a 12-month circle. M_i^{mod} and M_i^{obs} are the predicted and observed phases respectively.

Benchmark: $\text{MAD} \leq 2$.

E Calculations for Carbon Emitted into Atmosphere from Model Training/Inference

E.1 Key inputs and assumptions

- **Service-unit (SU) charging on HPC software.** CPU queues are charged at 2 SU $\text{core}^{-1} \text{h}^{-1}$, the V100 queue at 3 SU per “resource*hour”, and the A100 queue at 4.5 SU $\text{resource}^{-1} \text{h}^{-1}$.
- **Hardware power draw.**
 - CPU node $P_{\text{system}} = 2.90 \text{ MW}$, i.e. $P_{\text{core}} = 14.2 \text{ W}$.
 - DGX A100 node. $P_{\text{node}} = 6.5 \text{ kW}$ for 8×A100 GPUs¹⁹ $\Rightarrow P_{\text{GPU}} = 0.81 \text{ kW}$.
 - DGX-1 V100 node. Thermal-design power $P_{\text{node}} = 3.2 \text{ kW}$ for 8×V100 GPUs $\Rightarrow P_{\text{GPU}} = 0.40 \text{ kW}$.
- **Data-centre overhead.** Power-usage-effectiveness (PUE) assumed $\text{PUE} = 1.3^{20}$.
- **Grid-emission factor** Scope-2 factor $0.68 \text{ kg CO}_2 \text{ kWh}^{-1}$ and scope-3 factor $0.05 \text{ kg CO}_2 \text{ kWh}^{-1}$ from the Combined factor used below: $\gamma = 0.73 \text{ kg CO}_2 \text{ kWh}^{-1}$.

E.2 CPU workloads

Energy per core-hour $E_{\text{core}} = P_{\text{core}} \times \text{PUE} = 14.2 \text{ W} \times 1.3 = 18.5 \text{ W} = 0.0185 \text{ kWh}$.

SU-to-energy conversion CPU: 2 SU per core-hour, hence $E_{\text{SU}} = 0.0185 \text{ kWh}/2 = 9.25 \times 10^{-3} \text{ kWh}$.

Carbon per kSU 1 kSU = 1 000 SU $\Rightarrow m_{\text{kSU}} = 1 000 E_{\text{SU}} \gamma = 1 000 \times 9.25 \times 10^{-3} \times 0.73 \approx 6.8 \text{ kg CO}_2 \text{ e}$.

E.3 GPU workloads

A100

$$\begin{aligned} E_{\text{GPU h}} &= P_{\text{GPU}} \times \text{PUE} = 0.8125 \text{ kW} \times 1.3 = 1.06 \text{ kWh}, \\ m_{\text{GPU h}} &= E_{\text{GPU h}} \gamma \approx 1.06 \times 0.73 = 0.77 \text{ kg CO}_2 \text{ e}. \end{aligned}$$

Six-hour run on a single A100: $m = 6 \times 0.77 \approx 4.6 \text{ kg CO}_2 \text{ e}$.

V100

$$\begin{aligned} E_{\text{GPU h}} &= 0.40 \text{ kW} \times 1.3 = 0.52 \text{ kWh}, \\ m_{\text{GPU h}} &= 0.52 \times 0.73 = 0.38 \text{ kg CO}_2 \text{ e}. \end{aligned}$$

One hour per V100: $0.38 \text{ kg CO}_2 \text{ e}$.

¹⁹See A100 power draw per nvidia specifications: <https://www.nvidia.com/content/dam/en-zz/Solutions/Data-Center/nvidia-dgx-a100-datasheet.pdf>

²⁰Specific to local cluster

E.4 Summary

Workload	Energy (kWh h ⁻¹)	CO ₂ (kg h ⁻¹)
CPU	0.0185	0.014
A100 GPU	1.06	0.77
V100 GPU	0.52	0.38

These values were scaled for the various runtimes involved in each script.

F Chain-rule proof of the KL-decomposition

Note that the terminology and logic here is adapted from [31] [30] but has been adapted for the downscaling setting.

Throughout we write λ_d for the d -dimensional Lebesgue measure, (i.e. the ordinary notion of volume for a distribution in \mathbb{R}^d - we only define this here to get some nice continuity guarantees for our marginals later)

Formally, a probability law q on \mathbb{R}^d is said to be *absolutely continuous* with respect to λ_d , written $q \ll \lambda_d$, if there exists a non-negative integrable function $q(x)$ —the *density*—such that $q(A) = \int_A q(x) dx$ for every measurable set A . Absolute continuity is what licenses the familiar integral form of the Kullback–Leibler divergence $KL(q||p) = \int q(x) \log \frac{q(x)}{p(x)} dx$.

In the hierarchical-diffusion setting the fine and coarse image tensors live in Euclidean spaces

$$\mathcal{X} = \mathbb{R}^{h_{t-1} \times w_{t-1} \times C}, \quad \mathcal{Y} = \mathbb{R}^{h_t \times w_t \times C},$$

so we denote their Lebesgue measures by $\lambda_{\mathcal{X}}$ and $\lambda_{\mathcal{Y}}$, respectively. Assuming $q_{t-1}, p_{t-1} \ll \lambda_{\mathcal{X}}$ and $q_t, p_t \ll \lambda_{\mathcal{Y}}$ simply states that all four distributions possess densities, allowing us to manipulate KL integrals rigorously.

The decomposition proved below is the *chain rule of relative entropy*, first written explicitly by Kullback & Leibler [21] and now standard in information theory [6]. We give the brief self-contained derivation here for completeness and to show notation for the downscaling/super-resolution setting.

Throughout we let $\mathcal{X} = \mathbb{R}^{h_{t-1} \times w_{t-1} \times C}$ and $\mathcal{Y} = \mathbb{R}^{h_t \times w_t \times C}$ denote the fine- and coarse-resolution spaces at step t , and we assume $q_{t-1}, p_{t-1} \ll \lambda_{\mathcal{X}}$ and $q_t, p_t \ll \lambda_{\mathcal{Y}}$ for the appropriate Lebesgue measures (absolute continuity guarantees the existence of densities).

Let the deterministic down-sampling operator be $D_t : \mathcal{X} \rightarrow \mathcal{Y}$ and write $Y = D_t(X)$. Because D_t is measurable and information–non-increasing, the push-forwards $q_t := D_t \# q_{t-1}$ and $p_t := D_t \# p_{t-1}$ exist and are again absolutely continuous.

[KL chain rule under a measurable map] For any pair of measures q_{t-1}, p_{t-1} on \mathcal{X} and any measurable mapping $D_t : \mathcal{X} \rightarrow \mathcal{Y}$,

$$KL(q_{t-1} || p_{t-1}) = KL(q_t || p_t) + E_{y \sim q_t} \left[KL(q_{t-1} | Y=y || p_{t-1} | Y=y) \right], \quad (15)$$

where the inner KL is taken between the regular conditional distributions of X given $Y = y$. Both terms on the right-hand side are non-negative, hence splitting the coarse-scale divergence from the fine-scale residual.

Proof. Let $p(x), q(x)$ be the densities of p_{t-1}, q_{t-1} w.r.t. $\lambda_{\mathcal{X}}$, and denote the joint law of (X, Y) under q by $q(x, y) = q(x) \delta(y - D_t(x))$, with an analogous definition for p . Because Y is a deterministic function of X , we may factorise $q(x) = q(y) q(x|y)$ and $p(x) = p(y) p(x|y)$, where $q(y)$ and $p(y)$ are the coarse densities and $q(x|y), p(x|y)$ are the conditional densities.

Using $KL(q||p) = \int q(x) \log \frac{q(x)}{p(x)} dx$ and substituting the factorisations,

$$\begin{aligned} KL(q||p) &= \int q(y) q(x|y) \left[\log \frac{q(y)}{p(y)} + \log \frac{q(x|y)}{p(x|y)} \right] dx dy \\ &= \int q(y) \log \frac{q(y)}{p(y)} dy + \int q(y) \left[\int q(x|y) \log \frac{q(x|y)}{p(x|y)} dx \right] dy. \end{aligned}$$

The first integral is $KL(q_t \| p_t)$; the term in square brackets is $KL(q_{t-1} | Y=y \| p_{t-1} | Y=y)$. Taking the expectation over $y \sim q_t$ gives Eq. (15). \square

Consequence for the HDD process. Setting $Y = D_t(X)$ and identifying q_{t-1}, p_{t-1} with the forward and reverse marginals at scale $h_{t-1} \times w_{t-1}$ yields exactly Eq. (14) of the main text:

$$KL(q_{t-1} \| p_{t-1}) = \underbrace{KL(D_t q_{t-1} \| D_t p_{t-1})}_{\text{coarse term}} + E_{x_t \sim q_t} KL(q_{t-1} | x_t \| p_{t-1} | x_t).$$

Because the conditional KL is non-negative, matching the down-sampled marginals can only reduce the divergence at the fine scale, proving the monotone-improvement property stated in Theorem 3.1. \square

G Additional Results and Hyperparameters

We also included the CRPS metric calculated over 20 ensemble runs for the Base EDM and the HDD model for the results calculated in table 1 in the experiments section. We restrict these to the two equivalent 50 step runs to reduce computational load for large ensembles.

Table 6: Results extended to include CRPS metric. HDD reports values over a probabilistic distribution which are closer to the true underlying value

Model	RMSE	PSNR	CRPS
Base EDM – 50 Steps	0.000197	29.17	0.0002415
HDD – 50 steps – 3 denoise steps per shape step	0.000157	31.40	0.0002402

Below we summarise the key hyperparameters used for sampling and inference in our experiments:

Table 7: Hyperparameters used for sampling and inference. Note that these were generally kept the same as the original EDM implementation in [17]

Hyperparameter	Value
<i>Inference sampling</i>	
Number of steps	50 ²¹
<i>Noise schedule</i>	
σ_{\min}	0.002
σ_{\max}	80
ρ	7
<i>Stochasticity (churn)</i>	
S_{churn}	1
S_{\min}	0
S_{\max}	$+\infty$
S_{noise}	1
<i>Hierarchical scheduler</i>	
Full resolution (H, W)	(144, 272)
Noise steps per split	1 - 50
<i>Hardware & batch</i>	
GPU	A100
Batch size	1